Physics of Fluids

RESEARCH ARTICLE | JANUARY 03 2023

Numerical modeling of a wire mesh for aerodynamic noise reduction

Shuai Li (李帅) ; Lars Davidson ; Shia-Hui Peng

Physics of Fluids 35, 015103 (2023)
https://doi.org/10.1063/5.0129284

Physics of Fluids ARTICLE scitation.org/journal/phf

Numerical modeling of a wire mesh for aerodynamic noise reduction

Cite as: Phys. Fluids **35**, 015103 (2023); doi: 10.1063/5.0129284
Submitted: 4 October 2022 · Accepted: 7 December 2022 ·
Published Online: 3 January 2023

Shuai Li (李帅),[1,a)] Lars Davidson,[1] and Shia-Hui Peng[1,2]

AFFILIATIONS

[1]Division of Fluid Dynamics, Department of Mechanics and Maritime Sciences, Chalmers University of Technology, SE-412 96 Gothenburg, Sweden
[2]FOI, Swedish Defense Research Agency, SE-164 90 Stockholm, Sweden

[a)]Author to whom correspondence should be addressed: shuai.li@chalmers.se

ABSTRACT

A novel wire mesh consisting of very fine wires and pores is numerically investigated for the purpose of noise reduction. To develop a numerical model for this wire mesh, a set of experimental flow-field data has been deployed for the model validation. The experimental data were measured with only 22% of the wind-tunnel cross section covered by the wire mesh, taking into account the vortex shedding from both sides of the wire-mesh fairing. It is found that existing wire-mesh models using a damping-type source term proportional to the square of flow velocity do not perform well in modeling this novel wire mesh. To tackle this issue, an improvement is proposed by additionally introducing a linear term to account for the permeability of the wire mesh, based on another set of experiments with the wind-tunnel cross section fully covered by the wire mesh. The proposed model is then validated against the experimental data, demonstrating its capability in modeling the wire mesh. Subsequently, the model is applied to a tandem cylinder configuration. Results show that a wide but short-span wire mesh significantly reduces the dominant tone of tandem cylinders, noise at higher frequencies, as well as the overall sound pressure levels.

I. INTRODUCTION

With the continuous increase in air transportation over the past several decades, aircraft noise has become a more pressing topic of concern.[1] During approach and landing phases, landing gear noise, mostly generated by the interaction of turbulent flows with aircraft landing gears (LG), is one of the main contributors to the aircraft noise in the vicinity of airports. The development of effective noise reduction techniques (NRTs) is, thus, of paramount importance to the design of next generation quieter landing systems for business jets and transport aircrafts.

Perforated fairings have been demonstrated to be an impressive NRT for landing gear noise.[2–5] Among the various NRTs for landing gear noise, fairings probably have the highest technology readiness level (TRL).[6] Particularly, wire meshes have been investigated in some European Union's projects, e.g., the technologies to improve airframe noise (TIMPAN), the advanced low noise landing (main and nose) gear for regional aircraft (ALLEGRA), the highly accurate/reliable WT test demonstration of low-noise innovative MLG configuration (ARTIC), the innovative methodologies and technologies for reducing aircraft noise generation and emission (IMAGE), and the innovative design of installed airframe components for aircraft noise reduction (INVENTOR) projects. The work carried out in this paper is part of the on-going INVENTOR project. Indeed, in these and many other previous studies, the mechanism using wire meshes for bluff-body noise reduction has intensively been explored. As summarized by Zhao *et al.*,[6] this is associated with three possible aspects, all interfering with bluff-body flow aerodynamics. First, meshes reduce local impinging flow velocities; second, meshes may break up the incoming flow into small-scale vortices so that spanwise coherent vortices shedding from the bluff body are altered;[7] and third, meshes may move the vortex shedding away from bluff-body surfaces, thus reducing the acoustic radiation efficiency.

Wind-tunnel experiments were conducted to study the performances of wire meshes on LG noise reduction in the framework of the TIMPAN project.[8,9] Oerlemans *et al.*[8] performed acoustic and resistance tests on wire meshes of different materials (aluminum, steel, and nonmetallic materials), different wire and pore dimensions, and different shapes for LG noise reduction in NLR's Small Anechoic Wind Tunnel in the Netherlands. It was found that the wire meshes yielded a drastic broadband noise reduction for a wide range of mesh materials and shapes. Smith *et al.*[9] conducted tests on a 1/4 scale model of a main landing gear for a long-range aircraft in the QinetiQ NTF test

facility, with wire meshes used. The measured noise data were then transposed to flight conditions, showing that a reduction of more than 3 effective perceived noise decibel (EPNdB) noise was achieved for a main landing gear during approach and that the total aircraft noise was reduced by 0.8 EPNdB.[9]

Although wind-tunnel tests can be performed to study the noise reduction effects and mechanisms of wire meshes, they are very expensive. Numerical simulations coupled with an acoustic analogy are the most commonly adopted approach. The biggest challenge of numerical simulations, however, is that the openings of wire meshes are often very small in comparison with real-world industrial geometries. Such large difference in dimensions between the real-world geometry and the wire-mesh pores (which generate much finer eddies downstream the wire meshes) makes detailed meshing of the real-world geometry and the wire mesh not practical since it will result in a large amount of computational cells. It is, thus, industrially impractical to resolve wire meshes in numerical simulations. A numerical model for wire meshes is imminently favored.

For its computational effectiveness, numerical modeling of wire meshes has attracted increasing attention for bluff-body noise reduction. There are numerous ways to model the effect of wire meshes. Chen and Li[10] modeled the wire mesh as an array of identical tiny circular cylinders arranged in parallel. Okolo *et al.*[11] modeled the flow through woven wire meshes as laminar flow. The decay of turbulence quantities downstream of the screens was then taken into account with the aid of a suitably selected turbulence model that best replicates the experimental data. Okolo *et al.*[12] modeled the effect of three-dimensional (3D) wire-mesh screens by using staggered cylinders as an approximate two-dimensional (2D) simplification, resulting in satisfactory velocity field, pressure loss, and turbulence intensity in comparison with both experiments and 3D simulations. This provides the possibility of studying the effect of wire-mesh screens upstream or wrapped around 2D shapes for flow and noise control, thus significantly reducing simulation costs. Most often, the flow-through wire meshes are modeled using a damping-type source term in the momentum equations,[13–15] sometimes together with turbulence alterations or modeling to account for the turbulence generated downstream the wire meshes.[16–18] To determine the resistance coefficient, these wire-mesh models rely on the use of empirical formulas which were proposed based on measurements in a wind tunnel with the tunnel cross section fully covered by a wire mesh,[19,20] i.e., with the four sides of the wire mesh blocked by the wind-tunnel walls [see Fig. 1(a)]. However, in practical LG applications, wire meshes are often deployed and exposed to freestream in an open area. It is, thus, for this reason that a set of tests with only 22% of the tunnel cross section covered by a wire mesh [see Fig. 1(b)], taking into account the vortex shedding from the wire-mesh fairing side edges, are conducted in the framework of the on-going INVENTOR project. In the present study, a novel wire-mesh model is proposed and validated against these measurements. The model is then applied to a tandem cylinder configuration to assess its performance in noise reduction.

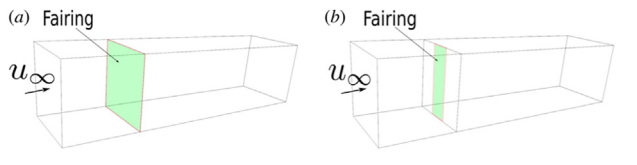

FIG. 1. Sketch of a fairing in a wind tunnel: (a) with the wind-tunnel cross section fully covered by the fairing and (b) with only 22% of the wind-tunnel cross section covered by the fairing.

In this paper, we model a novel dense wire mesh consisting of very fine wires and pores. This wire mesh was fabricated by the German Aerospace Center (DLR) and is hereinafter called the DLR wire mesh. The DLR wire mesh has shown significant capabilities in LG noise reduction. Indeed, fine wire meshes are also widely deployed in acoustic liners for aircraft engine noise reduction.[10,21] Although a source term for the momentum equations, proportional to the square of flow velocity, has been proposed and successfully applied to model wire meshes with relatively large wires and lattices,[14,15] it is found that these existing models do not perform well in modeling the novel DLR wire mesh. Such a limitation has, thus, motivated the introduction of an additional linear term, proportional to the flow velocity, to the source term of the momentum equations. The physical logic behind this is that in the experimental configuration with only 22% of the wind-tunnel cross section covered by a wire mesh, the air does not fully pass through the wire-mesh fairing. Rather, a significant portion of the air passes over the wire-mesh fairing from the fairing side edges. In this case, the portion of air passing through the pores of the fairing may play a role, which is related to the permeability. The additionally introduced linear term here is a characterization of the permeability of the wire mesh. Indeed, as also indicated by Rice,[21] the small pore size causes a large part of the pressure drop to be governed by laminar flow conditions and, thus, provides a fairly linear resistance.

The paper is organized as follows: Sec. II is devoted to a description of the experimental data used for the validation of our wire-mesh model and for determining the model parameters. The details of the numerical setup and numerical methods are also described in this section. The limitation of the existing wire-mesh models, followed by an improved model proposed in this study, is described in Sec. III. The proposed wire-mesh model is then validated against the experiments in Sec. IV. In Sec. V, the model is applied to a tandem cylinder configuration to assess its performance in noise reduction. Finally, concluding remarks are summarized in Sec. VI.

II. EXPERIMENTAL DATA AND NUMERICAL SETUP

A. Description of the experimental data

In the present study, experimental data, including mean flow, turbulence, and pressure drop, are used for the validation of our wire-mesh model and for determining the model parameters. They are measured in the wind tunnel for aeroacoustic boundary layer, including pressure gradient effect (WAABLIEF) at the von Karman Institute for Fluid Dynamics (VKI) and in the Aero-thermo-Acoustics Bench (B2A) at the Office National d'Etudes et de Recherches Aérospatiales (ONERA).

The WAABLIEF wind tunnel is an open-loop suction-type subsonic wind tunnel with a closed square test section of $250 \times 250\,\mathrm{mm}^2$. The straight square test section has a length of 2 m. This wind tunnel is a low-turbulence wind tunnel with the free-stream turbulence intensity below 0.5% (see Ref. 22). This wind tunnel has been specifically designed for aeroacoustic studies. The readers may refer to Ref. 22 for more details regarding this wind tunnel. In the present measurements, the fairing has a width of $L = 54\,\mathrm{mm}$ and a span of $H = 250\,\mathrm{mm}$ and is placed at 1.25 m from the entrance of the test section. The fairing

covers an area of 22% of the wind-tunnel cross section [see Fig. 1(b)]. The pressure drop is measured by placing a Pitot tube at $(x - x_{fairing})/L = -5.778$ upstream the fairing and three Pitot tubes downstream the fairing at $(x - x_{fairing})/L = 0.185$, 0.741, and 1.296, respectively. For a velocity at the wind-tunnel entrance $u_\infty = 16$ m/s, the pressure drop measured at the above-mentioned three locations are $\Delta p/(0.5\rho u_\infty^2) = 3.4991$, 4.0812, and 4.2791, respectively (see Ref. 23). The velocities are measured downstream the fairing using hot wires. The pressure drop, mean velocity, and turbulence intensity measured in the WAABLIEF wind tunnel will be used to validate our proposed numerical model for the DLR wire mesh.

The B2A wind tunnel is designed so that the static flow temperature can be accurately regulated from the ambient temperature up to 300 °C, with a mean flow bulk Mach number up to 0.5. A 0.2 m long test section is equipped with two silica windows for optical access. This wind-tunnel cross section has a dimension of $50 \times 50\,\text{mm}^2$. More details on the B2A wind tunnel can be found in Refs. 24 and 25. It is important to note that, in this experimental measurement, the fairing fully covers the entire cross section [see Fig. 1(a)]. In other words, the fairing has the same dimension as the wind-tunnel cross section, i.e., 50 mm in width and span. The pressure drop is measured by static pressure taps on the top of the test section upstream and downstream the fairing. For a velocity at the wind-tunnel entrance $u_\infty = 16.6$ m/s, the pressure drop measured in the B2A wind tunnel is $\Delta p/(0.5\rho u_\infty^2) = 56.883$ (see Ref. 25), and this measurement will be used to determine the parameters of our numerical model for the DLR wire mesh.

B. Numerical setup

The wire-mesh model proposed in the present study will be validated against the experiments conducted in the WAABLIEF wind tunnel. Figure 2(a) shows a wire-mesh fairing with a wire diameter of $d = 1$ mm and a spacing between wires of $s = 4$ mm (hereinafter called the ONERA wire mesh), leading to a porosity of $\beta = 0.64$. This wire mesh has been investigated numerically in the IMAGE project.[17,18] Figure 2(b) shows the DLR wire-mesh fairing with a diameter of $d = 0.042$ mm and a spacing between wires of $s = 0.14$ mm, leading to a porosity of $\beta = 0.59$. The DLR wire mesh has recently been tested to be very efficient in reducing LG noise in the framework of the ongoing INVENTOR project. Figure 2(c) shows the wire diameter d and the spacing between the wires s in a sketch.

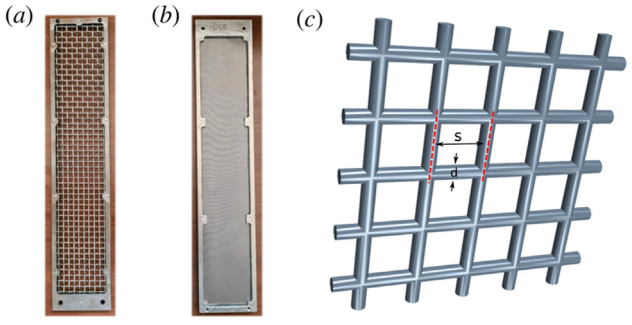

FIG. 2. Two different wire meshes: (a) ONERA wire mesh, (b) DLR wire mesh, and (c) sketch of an isolated wire mesh.

The simulated configuration here is a 1.0 m long channel with a square cross section of $250 \times 250\,\text{mm}^2$ [see Fig. 3(a)]. The velocity at the channel inlet is $u_\infty = 16$ m/s, corresponding to a Reynolds number of 132 000 based on the inlet velocity and the half-height of the channel. At the channel inlet, the velocity profile near the channel walls is prescribed according to the 1/7th power law.[22] Different number of cells in the streamwise direction (and, thus, different thicknesses) are used to represent the wire-mesh fairing. Four different time steps of $\Delta t = 1.0 \times 10^{-3}$, 1.0×10^{-4}, 1.1×10^{-4} (time step used for pyCALC-LES simulations only), and 1.0×10^{-5} s are used in the simulations. Similar to the WAABLIEF experiments, in numerical simulations, the wire-mesh fairing has a width of $L = 54$ mm and a span of $H = 250$ mm.

Table I shows nine computational meshes of different resolution in the present study. Except Mesh 5, the meshes are refined at and around the fairing, i.e., the minimum cell size in the streamwise direction $\Delta x_{\min}$ occurs at $x/L_{ch} = 0.25$ where L_{ch} is the length of the channel, i.e., $L_{ch} = 1$ m. Then, the meshes are stretched gradually in the streamwise direction and maximum $\Delta x_{\max}$ occurs at the furthest upstream and downstream locations in the computational domain. Figure 3(b) shows a structured computational mesh (Mesh 1) with grid refinement at $x/L_{ch} = 0.25$. In the channel flow simulations performed in this paper, unless shown in the figure legends, Mesh 1 is used. In the present study, the fairing mid-plane is located at $x/L_{ch} = 0.25$, $0 < y/H < 1$, $0.392 < z/H < 0.608$.

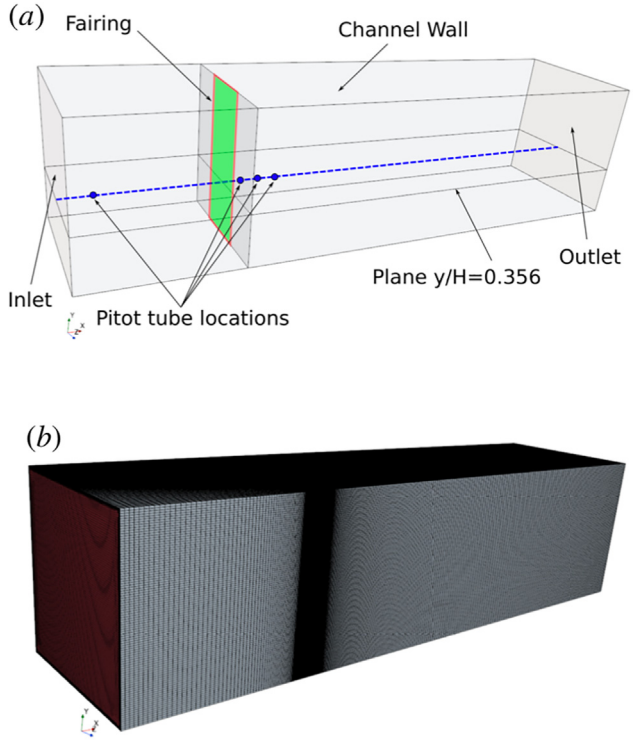

FIG. 3. The numerical setup in the present study: (a) computational domain and (b) computational mesh (Mesh 1). The blue dashed line in (a) is a line at the intersection of planes $y/H = 0.356$ and $z/H = 0.5$. The mean streamwise velocity, turbulence intensity, and pressure drop were measured along this line in the WAABLIEF wind tunnel.

TABLE I. Computational meshes for channel flows. The cell dimensions Δx, Δy, and Δz listed in this table are in millimeter (mm). The total number of cells in the last column are in million (M). Δy and Δz listed here are dimensions of cells away from the channel walls. In the near-wall regions, meshes 1–5 include prism layers with $y^+ < 1$. Wall functions were applied at all channel walls for meshes 6–9 with $y^+ = 30$.

Mesh	$\Delta x_{\min}$	$\Delta x_{\max}$ (u/d)[a]	Δy	$\Delta z_{\min}$	$\Delta z_{\max}$	# M. cells
1	0.042	5.0/5.0	2.7	2.7	2.7	6.4
2	0.0084	6.0/7.0	2.7	2.7	2.7	8.0
3	1.0	5.0/5.0	2.7	2.7	2.7	6.4
4	1.0	2.7/2.7	2.7	2.7	2.7	5.6[b]
5	2.7	2.7/2.7	0.9	0.9	0.9	35.0
6	0.65	4.0/4.0	1.9	0.65	4.0	6.5
7	0.65	4.0/2.7	1.9	1.9	1.9	6.9
8	0.65	4.0/4.0	1.9	0.65	2.0	8.9
9	1.0	4.0/4.0	1.9	1.0	2.0	18.4

[a]Maximum Δx at the furthest upstream and downstream.
[b]Unstructured polyhedral mesh. Except this mesh, other meshes are structured meshes.

We perform large-Eddy simulations (LES) with the wall-adapting local Eddy-viscosity (WALE) subgrid-scale model. The simulations are performed using the commercial Siemens STAR-CCM+ version 2021.1[26] and the in-house code pyCALC-LES.[27] For the STAR-CCM+, the readers may refer to the user guide for the numerical algorithms.[28] In this study, the Navier–Stokes equations are solved in a coupled manner. An implicit, second-order, three-level Euler scheme is used for the time integration. For the pyCALC-LES, it is an incompressible finite-volume code. It is fully vectorized without "for" loops. The solution procedure is based on fractional step. The discretization in space is a combination of central differencing (95%) and MUSCL (5%). MUSCL is a second-order upwind scheme. The Crank–Nicolson scheme is used in time marching. More details of the numerical methods are given in Sec. II C.

C. Numerical methods for the solvers

1. STAR-CCM+

In STAR-CCM+, the discretized governing equation of fluid flow can be written as[28]

$$\frac{d}{dt}(\rho\phi V)_0 + \sum_f [\rho\phi(\vec{u}\cdot\vec{a})]_f = \sum_f [\Gamma\nabla\phi\cdot\vec{a}]_f + (S_\phi V)_0, \quad (1)$$

where the subscript "0" denotes the quantities at the cell center of a finite control volume and the subscript "f" represents the quantities at the cell face. V is the volume of the cell and $\vec{a}$ is the surface area vector of face f of the cell. By setting ϕ equal to 1, u_1, u_2, u_3, or E and selecting appropriate values for the diffusion coefficient Γ and source term S_ϕ, the equations for mass, momentum, and energy conservation can be obtained. From left to right, the four terms in Eq. (1) represent the transient term, convective flux, diffusive flux, and source term.

The discretized convective flux at a face can be rearranged as follows:

$$(\rho\phi\vec{u}\cdot\vec{a})_f = (\dot{m}\phi)_f = \dot{m}_f\phi_f, \quad (2)$$

where $\dot{m}_f$ is the mass flow rate at the face. The bounded central-differencing (BCD) scheme is used to approximate the convective flux as

$$(\dot{m}\phi)_f = \begin{cases} \dot{m}\phi_{FOU} & \text{if } \xi < 0 \text{ or } \xi > 1 \\ \dot{m}[\sigma\phi_{CD} + (1-\sigma)\phi_{SOU}] & \text{if } 0 \le \xi \le 1, \end{cases} \quad (3)$$

where ϕ_{FOU}, ϕ_{CD}, and ϕ_{SOU} are cell-face center values obtained through first-order upwind, central-differencing, and second-order upwind interpolation, respectively. ξ is the normalized-variable diagram (NVD) value that is computed based on local conditions. σ is a smooth and monotone function of ξ, i.e., $\sigma = \sigma(\xi)$, which satisfies $\sigma(0) = 0$ and $\sigma(\xi) = 1$ for $\xi_{ubf} < \xi$. ξ_{ubf} is the upwind blending factor whose value ensures a proper balance between the accuracy and robustness of the scheme.[28]

For the diffusive flux, to obtain an accurate second-order expression for an interior face gradient that implicitly involves the cell values ϕ_0 and ϕ_1, the following decomposition is used:

$$\nabla\phi_f = (\phi_1 - \phi_0)\vec{\alpha} + \overline{\nabla\phi} - (\overline{\nabla\phi}\cdot d\vec{s})\vec{\alpha}, \quad (4)$$

where

$$\vec{\alpha} = \frac{\vec{a}}{\vec{a}\cdot d\vec{s}}, \quad (5)$$

$$d\vec{s} = \vec{x}_1 - \vec{x}_0, \quad (6)$$

$$\overline{\nabla\phi} = \frac{(\nabla\phi_0 + \nabla\phi_1)}{2}. \quad (7)$$

The diffusive flux at an interior face can then be written as

$$(\Gamma\nabla\phi\cdot\vec{a})_f = \Gamma_f\left[(\phi_1 - \phi_0)\vec{\alpha}\cdot\vec{a} + \overline{\nabla\phi}\cdot\vec{a} - (\overline{\nabla\phi}\cdot d\vec{s})\vec{\alpha}\cdot\vec{a}\right], \quad (8)$$

where Γ_f is a harmonic average of the cell values.

For the transient term, an implicit, second-order, three-level Euler scheme is used for the time integration as follows:

$$\frac{d}{dt}(\rho\phi V)_0 = \left(\frac{3}{2}(\rho\phi V)_0^{n+1} - 2(\rho\phi V)_0^{n} + \frac{1}{2}(\rho\phi V)_0^{n-1}\right)\frac{1}{\Delta t}, \quad (9)$$

where $n+1$ is the current time level, n and $n-1$ are the previous two time levels, and Δt is the time step.

2. pyCALC-LES

The filtered incompressible Navier–Stokes equation for LES reads

$$\frac{\partial\tilde{u}_i}{\partial t} + \frac{\partial\tilde{u}_i\tilde{u}_j}{\partial x_j} = -\frac{\partial\tilde{p}}{\partial x_i} + \nu\frac{\partial^2\tilde{u}_i}{\partial x_j\partial x_j} - \frac{\partial\tau_{ij}^r}{\partial x_j}, \quad (10)$$

where ν is the kinematic viscosity and τ_{ij}^r is the anisotropic residual stress tensor.[27,29] The discretized equation reads

$$\tilde{u}_i^{n+1/2} = \tilde{u}_i^n + \Delta t H\left(\tilde{u}_i^n, \tilde{u}_i^{n+1/2}\right) - \alpha\Delta t\frac{\partial\tilde{p}^{n+1/2}}{\partial x_i} - (1-\alpha)\Delta t\frac{\partial\tilde{p}^n}{\partial x_i}, \quad (11)$$

where H includes convective, viscous, and subgrid-scale terms. The convective terms are discretized using 95% central differencing and

5% MUSCL. The face velocities $\tilde{u}_{f,i}^{n+1/2} = 0.5(\tilde{u}_{i,j}^{n+1/2} + \tilde{u}_{i,j-1}^{n+1/2})$ (note that j denotes node number and i is a tensor index) do not satisfy continuity. Create an intermediate velocity field by subtracting the implicit pressure gradient from Eq. (11), i.e.,

$$\tilde{u}_i^* = \tilde{u}_i^n + \Delta t H\left(\tilde{u}_i^n, \tilde{u}_i^{n+1/2}\right) - (1-\alpha)\Delta t \frac{\partial \tilde{p}^n}{\partial x_i}, \tag{12a}$$

$$\Rightarrow \tilde{u}_i^* = \tilde{u}_i^{n+1/2} + \alpha \Delta t \frac{\partial \tilde{p}^{n+1/2}}{\partial x_i}. \tag{12b}$$

Take the divergence of Eq. (12b) and require that $\partial \tilde{u}_{f,i}^{n+1/2}/\partial x_i = 0$ so that

$$\frac{\partial^2 \tilde{p}^{n+1}}{\partial x_i \partial x_i} = \frac{1}{\alpha \Delta t}\frac{\partial \tilde{u}_{f,i}^*}{\partial x_i}. \tag{13}$$

The Poisson equation for $\tilde{p}^{n+1}$ is solved and then the face velocities are corrected as

$$\tilde{u}_{f,i}^{n+1} = \tilde{u}_{f,i}^* - \alpha \Delta t \frac{\partial \tilde{p}^{n+1}}{\partial x_i}. \tag{14}$$

The solution procedure may be summarized as below.

1. Solve the discretized filtered Navier–Stokes equation, Eq. (12a), for $\tilde{u}_1$, $\tilde{u}_2$, and $\tilde{u}_3$;
2. Create an intermediate velocity field $\tilde{u}_i^*$ from Eq. (12b);
3. Use linear interpolation to obtain the intermediate velocity field, $\tilde{u}_{f,i}$, at the face;
4. The Poisson equation Eq. (13) is solved;
5. Compute the face velocities (which satisfy continuity) from the pressure and the intermediate face velocity from Eq. (14);
6. The eddy viscosity is computed by the WALE model;
7. Convergence is obtained on one iteration: next time step.

The discretized momentum and Poisson equations are solved on the graphics processing unit (GPU) using the pyamgx solver.

III. WIRE-MESH MODELING

A. Existing wire-mesh models

In classical wire-mesh models, the effect of wire meshes on flows is modeled using a damping-type source term in the momentum equations.[13–18] Within the wire-mesh region, a volume-averaged source term S is added to the right-hand side (RHS) of the momentum equations to model the effect of wire meshes, yielding the compressible LES momentum equations for filtered velocity $\tilde{u}_i$ as

$$\frac{\partial(\rho \tilde{u}_i)}{\partial t} + \frac{\partial(\rho \tilde{u}_i \tilde{u}_j)}{\partial x_j} = -\frac{\partial \tilde{p}}{\partial x_i} + \frac{\partial \tilde{\sigma}_{ij}}{\partial x_j} + \frac{\partial \sigma_{ij,SGS}}{\partial x_j} + S_i, \tag{15}$$

where $\tilde{\sigma}_{ij}$ is the viscous stress tensor which can be expressed as

$$\tilde{\sigma}_{ij} = 2\mu \tilde{S}_{ij} - \frac{2}{3}\mu \tilde{S}_{kk}\delta_{ij}, \tag{16}$$

and the subgrid-scale stress tensor

$$\sigma_{ij,SGS} = 2\mu_t \tilde{S}_{ij} - \frac{2}{3}\mu_t \tilde{S}_{kk}\delta_{ij}, \tag{17}$$

where $\tilde{S}_{ij}$ is the strain rate tensor and can be written as

$$\tilde{S}_{ij} = \frac{1}{2}\left(\frac{\partial \tilde{u}_i}{\partial x_j} + \frac{\partial \tilde{u}_j}{\partial x_i}\right). \tag{18}$$

If the air flow approaches the wire mesh at zero incident angle, the source term is expressed as

$$\begin{bmatrix} S_1 \\ S_2 \\ S_3 \end{bmatrix} = \begin{bmatrix} -K_0 \times 0.5\rho|\tilde{u}|\tilde{u}/h \\ 0 \\ 0 \end{bmatrix}, \tag{19}$$

where h is the fairing thickness and the resistance coefficient K_0 is given by an empirical formula[20]

$$K_0 = \left(0.5 + \frac{26}{Re_d}\right)\left(\frac{1-\beta^2}{\beta^2}\right), \tag{20}$$

where the porosity β is expressed as

$$\beta = (1 - d/s)^2. \tag{21}$$

B. Limitation of the existing models

Using the classical model in Eq. (19), Fig. 4 shows the mean streamwise velocity and turbulent intensity along the line at the intersection of Planes $y/H = 0.356$ and $z/H = 0.5$. According to Zamponi *et al.*,[30] the turbulent intensity is defined as

$$u' = \sqrt{[(u-\bar{u})\cos\alpha]^2 + [(v-\bar{v})\cos\alpha]^2}, \tag{22}$$

where α is

$$\alpha = \tan^{-1}\left(\frac{\bar{v}}{\bar{u}}\right). \tag{23}$$

In the mean streamwise velocity profile, a plateau exists from the fairing to a distance of L downstream the fairing. Then, the mean streamwise velocity decreases to a minimum value at $x/L = 6.7$. This plateau makes the numerical prediction deviate from the experimental data. In terms of the turbulent intensity, the numerical prediction produces a similar trend as the experimental measurements. However, there still exists a small difference between the two. Figure 5 shows the pressure drop which has a big disparity between the numerical predictions and the experimental measurements at three locations downstream the wire mesh, i.e., $(x - x_{fairing})/L = 0.185$, 0.741, and 1.296.

C. An improved model for the DLR wire mesh

Considering the disparity of pressure loss between the WAABLIEF and the B2A measurements presented in Sec. II A, we separate the pressure loss caused by a wire mesh into two parts. On the one hand, a wire mesh, whether consisting of very fine pores (e.g., DLR wire mesh) or coarse pores (e.g., ONERA wire mesh), causes a quadratic pressure loss proportional to the square of flow velocity. On the other hand, the permeability of a wire mesh causes a linear pressure loss. For wire meshes consisting of coarse pores (e.g., ONERA wire mesh), the permeability is high and, therefore, the pressure loss caused by the permeability is small. For wire meshes consisting of very fine pores (e.g., DLR wire mesh), the permeability is low so that the

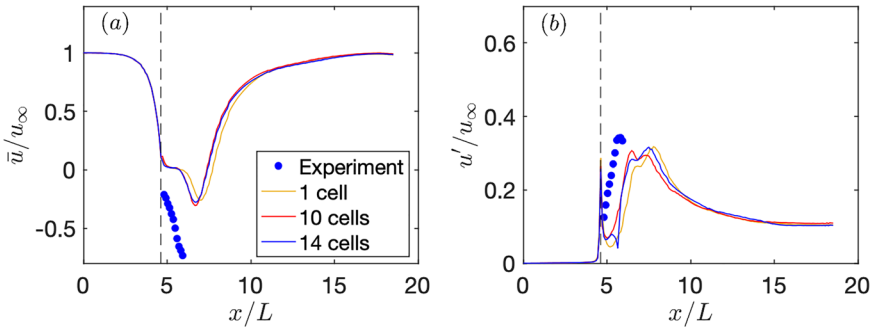

FIG. 4. Flow statistics along the line at the intersection of planes $y/H = 0.356$ and $z/H = 0.5$: (a) mean streamwise velocity and (b) turbulent intensity. In the simulations, the classical model in Eq. (19) is applied and different number of cells in the streamwise direction are used to represent the DLR wire mesh. The black dashed line indicates the position of the DLR wire mesh, i.e., $x/L = 4.63$.

pressure loss caused by the permeability becomes significant. This explains why the pressure loss measured in the B2A wind tunnel ($\Delta p/(0.5\rho u_\infty^2) = 56.883$) is significantly larger than that given by the empirical formulas ($\Delta p/(0.5\rho u_\infty^2) \approx 2.0$) for the DLR wire mesh, although the empirical formulas also came from experiments with the wind-tunnel cross section fully covered by wire meshes.[19,20] We, thus, propose an improvement to the classical models by additionally introducing a linear term to characterize the permeability of the DLR wire mesh as follows:

$$\begin{bmatrix} S_1 \\ S_2 \\ S_3 \end{bmatrix} = \begin{bmatrix} -\dfrac{\mu}{K_{perm}}\tilde{u} - \dfrac{K_0 \times 0.5\rho|\tilde{u}|\tilde{u}}{h} \\ 0 \\ 0 \end{bmatrix}, \tag{24}$$

where K_{perm} is a characterization of the permeability of wire meshes. Since K_{perm} is a characteristic of a porous medium, normally speaking, this parameter should be achieved from the fitting of many experimental data, like other porous media.[31–33] However, in this project, a large number of tests on the DLR wire mesh are not available. Therefore, it is not possible to determine K_{perm} through fitting here. It is, thus, a compromise to estimate K_{perm} based on the only available experimental data. In the B2A experiments, based on the fact that the pressure loss measured in the B2A wind tunnel is a combination of both the quadratic and the linear pressure losses, the pressure loss divided by h is

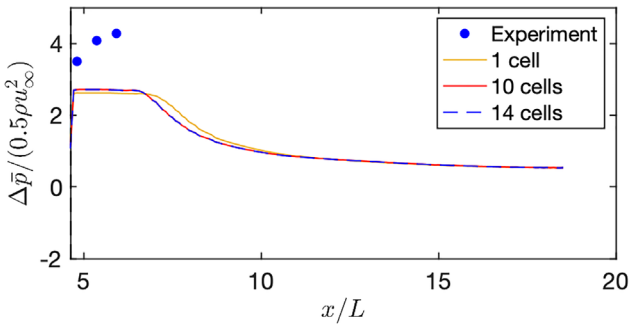

FIG. 5. Pressure drop along the line at the intersection of planes $y/H = 0.356$ and $z/H = 0.5$. In the simulations, the classical model in Eq. (19) is applied and different number of cells are used to represent the DLR wire mesh. The DLR wire mesh is located at $x/L = 4.63$, i.e., the y-axis.

$$\frac{\Delta p}{h} = \frac{\mu}{K_{perm}}u_\infty + \frac{K_0 \times 0.5\rho|u_\infty|u_\infty}{h}, \tag{25}$$

where the first and second terms on the right-hand side of Eq. (25) correspond to the linear pressure loss and quadratic pressure loss, respectively. Rice's work[21] also stated that the small pore size of fine wire screen causes a fairly linear resistance, strengthening our idea of adding a linear term in the momentum source. Since $\Delta p = K_{B2A} \times 0.5\rho u_\infty^2$, K_{perm} can be expressed as

$$K_{perm} = \frac{\mu u_\infty}{(K_{B2A} - K_0) \times 0.5\rho u_\infty^2/h}. \tag{26}$$

It should be noted that, by estimating K_{perm} in this way, the additional linear term is a correction based on the experimental data measured at the B2A wind tunnel. Results pertaining to the simulations using the improved model in Eqs. (24) and (26) are discussed in Sec. IV.

IV. RESULTS IN CHANNEL FLOWS

A. Effect of number of cells used to represent the fairing

In this subsection, we study the effect of number of cells used to represent the DLR wire-mesh fairing. We adopt 2, 4, 10, and 14 cells in the streamwise direction, corresponding to a thickness of 0.084, 0.17, 0.44, and 0.63 mm, respectively, compared to the actual fairing thickness of 0.042 mm. The simulations are performed using a time step of $\Delta t = 1 \times 10^{-3}$ s.

Figure 6 shows the mean streamwise velocity and turbulent intensity along the line at the intersection of planes $y/H = 0.356$ and $z/H = 0.5$ using the improved wire-mesh model. By introducing a linear term, the plateau in Fig. 4(a) disappears. With two cells used, the mean velocity profile agrees better with experimental data but the turbulent intensity does not. Since the curves obtained using two cells differ from other curves obtained using more cells, we conclude that the modeling does not converge when two cells are used, which is consistent with the results reported in Zhu *et al.*[14] With four or more cells used, very similar results are achieved. It is also clear that the curves obtained using 10 and 14 cells overlap, in both Figs. 6(a) and 6(b). Overall, although the turbulent intensity obtained using four or more cells agrees very well with the experimental data, the mean velocity differs, to some extent, from the experimental data. Particularly, the predicted minimum mean streamwise velocity are larger than that of the experimental data.

Figure 7 shows the pressure drop along the line at the intersection of planes $y/H = 0.356$ and $z/H = 0.5$ when the improved wire-

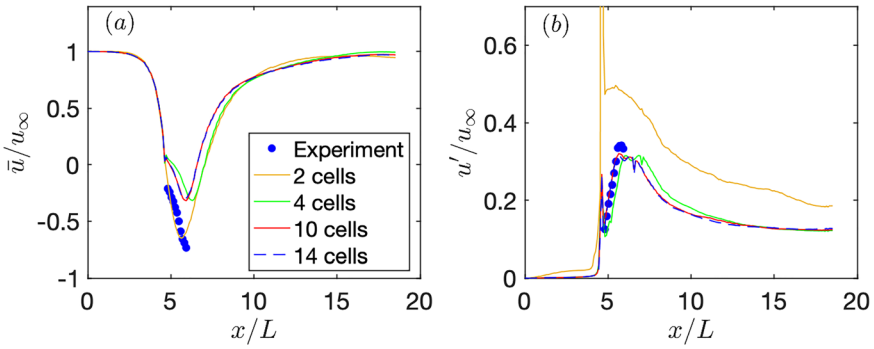

FIG. 6. Flow statistics along the line at the intersection of planes $y/H = 0.356$ and $z/H = 0.5$: (a) mean streamwise velocity and (b) turbulent intensity. In the simulations, the proposed model in Eqs. (24) and (26) is applied and different number of cells in the streamwise direction are used to represent the DLR wire mesh.

mesh model is applied. With two cells used, the profile of pressure drop agrees better with the experimental data. Similar to the mean streamwise velocity and turbulent intensity, the curves obtained using four or more cells get closer and those obtained using 10 and 14 cells overlap. It is also obvious that for the pressure drop to be as close as possible to the experimental measurements, a lower minimum in the profile of mean streamwise velocity should be obtained. Compared to the classical model, the proposed model has a higher plateau in pressure drop. However, the discrepancy between the numerical predictions and experimental measurements still exists. In Secs. IV C and IV D, we will see an improvement in the prediction of pressure drop when finer time steps are used.

Figure 8 shows a comparison of the time-averaged contours of the streamwise velocity, turbulent intensity, and pressure loss in plane $y/H = 0.356$ between the proposed model in Eqs. (24) and (26) and the classical model in Eq. (19). The quantities are normalized by the velocity at the channel inlet u_∞ and the dynamic pressure $P_{dyn} = 0.5\rho u_\infty^2$, respectively. Overall, the contours of both models are quite similar. However, the proposed model generates an earlier recirculation zone than the classical model does, as also seen in Figs. 4–7.

B. Effect of numerical thicknesses

Figure 9 shows the mean streamwise velocity and turbulent intensity along the line at the intersection of planes $y/H = 0.356$ and $z/H = 0.5$ when nonphysical and physical thicknesses are used to represent the DLR wire mesh. Here, physical thickness means that the thickness of the wire-mesh region, where the wire-mesh model is applied, is equal to the actual thickness of the wire mesh. The case when five cells are used on Mesh 2 corresponds to a thickness of 0.042 mm which is the physical thickness of the DLR wire mesh. The other two cases adopt 10 cells, but neither of them corresponds to the physical thickness. It is apparent that both physical thickness and nonphysical thickness produce highly similar results, suggesting that the proposed model is not significantly affected by whether or not the DLR wire mesh is represented with its actual physical thickness. Additionally, it is clear that with Mesh 2, the curves obtained using five cells overlap with those obtained 10 cells, suggesting that five cells are sufficient to represent the DLR wire mesh. Figure 10 shows the corresponding pressure drop. Expectedly, similar results for all cases are obtained. However, the discrepancy in pressure drop between numerical simulations and experimental measurements remains unchanged, even with the refined mesh and the physical thickness used.

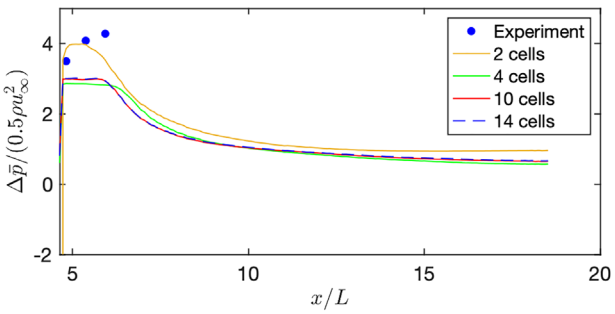

FIG. 7. Pressure drop along the line at the intersection of planes $y/H = 0.356$ and $z/H = 0.5$. In the simulations, the proposed model in Eqs. (24) and (26) is applied and different number of cells in the streamwise direction are used to represent the DLR wire mesh.

C. Effect of time steps

In this subsection, we decrease the time step from 1×10^{-3} to 1×10^{-4} and 1×10^{-5} s using 10 cells to represent the DLR wire mesh. Figure 11 shows the mean streamwise velocity and turbulent intensity along the line at the intersection of planes $y/H = 0.356$ and $z/H = 0.5$. On the one hand, a decrease in time step from 1×10^{-3} to 1×10^{-4} and 1×10^{-5} s produces better agreement with the experiment in terms of mean streamwise velocity. On the other hand, turbulent intensity slightly deviates from the experimental data. This is due to less numerical dissipation when a smaller time step is used. As a result, more turbulence is resolved, resulting in a stronger vortex shedding. The stronger vortex shedding generates an earlier recirculation region (or a shorter vortex-formation length). Figure 12 shows the pressure drop for three different time steps. As the time step decreases from 1×10^{-3} to 1×10^{-4} s, a slight increase in pressure drop is observed. A decrease in time step from 1×10^{-4} to 1×10^{-5} s further improves the prediction of pressure drop, particularly at the first location $(x - x_{fairing})/L = 0.185$ behind the fairing. Overall, a decrease in time step improves the results. It is, thus, suggested that it is better to use a time step at the level of 1×10^{-4} s or smaller, probably due to the very fine mesh used in the fairing-containing region.

D. Comparison between different solvers and meshes

In this subsection, we compare the predictions using different solvers and meshes. The time steps used in this comparison are

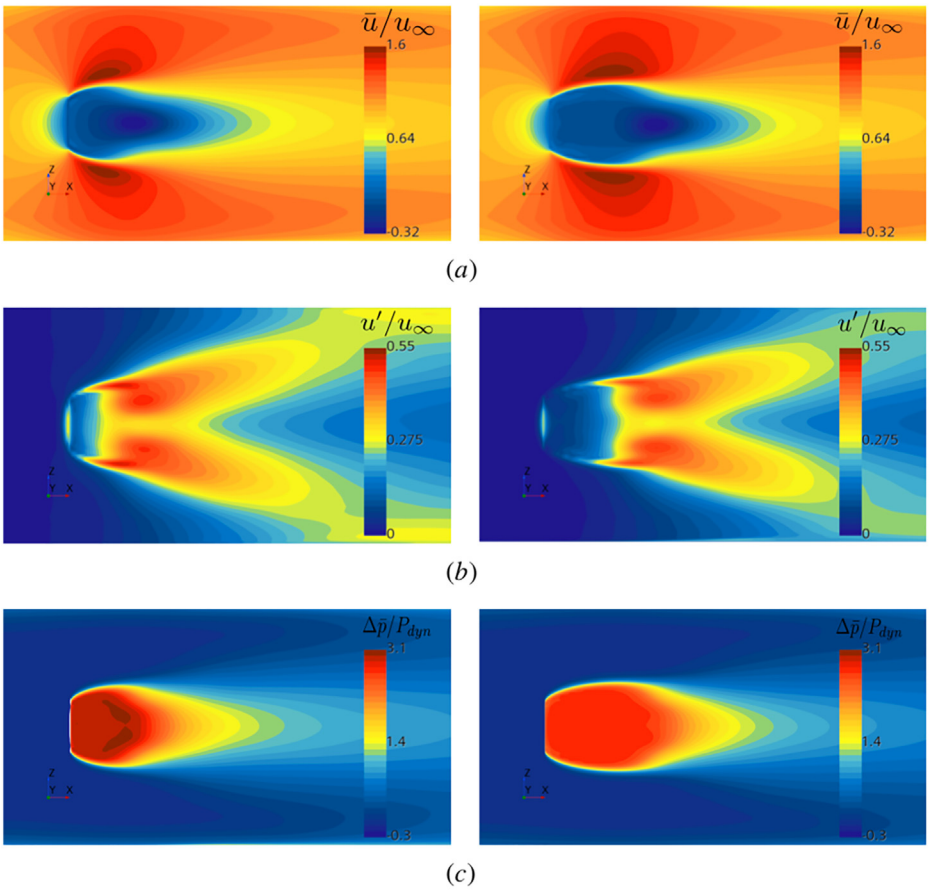

FIG. 8. Comparison of time-averaged contours in plane $y/H = 0.356$ between the proposed model in Eqs. (24) and (26) and the classical model in Eq. (19): (a) mean streamwise velocity ($\bar{u}/u_\infty$), (b) turbulent intensity (u'/u_∞), and (c) pressure loss ($\Delta\bar{p}/P_{dyn}$). Left column: the proposed model and right column: the classical model.

1×10^{-5} s for STAR-CCM+ and 1.1×10^{-4} s for pyCALC-LES, respectively. Figures 13 and 14 show the mean streamwise velocity, turbulent intensity and pressure drop when different solvers and meshes are used in the simulations. For both solvers, different meshes, including different grid resolution at the fairing and different types of meshes (e.g., structured and unstructured meshes), lead to very similar results in the mean streamwise velocity, turbulent intensity, and pressure drop, suggesting that the proposed model for the DLR wire mesh neither requires grid refinement at the fairing nor depends on mesh types as long as the total added force term is equal to each other in all simulations. Compared to the commercial STAR-CCM+, the in-house solver pyCALC-LES gives a delayed peak in the curves of pressure drop.

E. The DLR wire mesh modeled as a solid plate

In this subsection, we model the DLR wire mesh as a solid plate by applying a source term that is about 250 times stronger than the model in Eqs. (24) and (26).

Figure 15 shows the flow statistics along the line at the intersection of Planes $y/H = 0.356$ and $z/H = 0.5$. Apparently, the mean streamwise velocity and turbulent intensity hardly have differences in

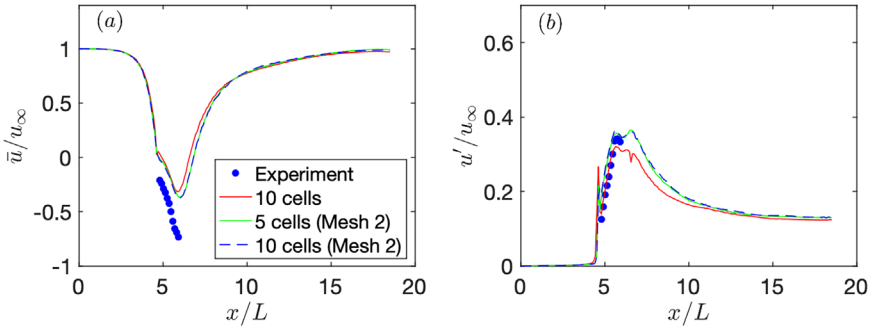

FIG. 9. Flow statistics along the line at the intersection of planes $y/H = 0.356$ and $z/H = 0.5$: (a) mean streamwise velocity and (b) turbulent intensity. In the simulations, the proposed model in Eqs. (24) and (26) is applied and both non-physical and physical thickness are used to represent the DLR wire mesh.

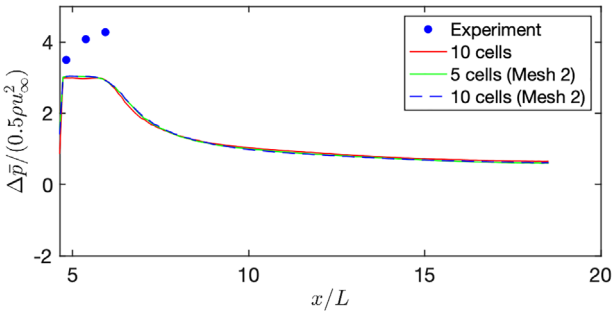

FIG. 10. Pressure drop along the line at the intersection of planes $y/H = 0.356$ and $z/H = 0.5$. In the simulations, the proposed model in Eqs. (24) and (26) is applied and both nonphysical and physical thickness are used to represent the DLR wire mesh.

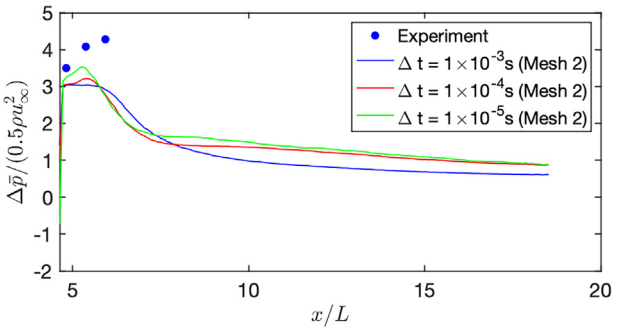

FIG. 12. Pressure drop along the line at the intersection of planes $y/H = 0.356$ and $z/H = 0.5$. In the simulations, the proposed model in Eqs. (24) and (26) is applied and three different time steps are used.

comparison to those in Fig. 13. However, the predicted pressure drop in Fig. 16 gets closer to the experimental measurements.

Figure 17 shows the contours of the mean streamwise velocity on the cross section at $x = x_{fairing}$ when the DLR wire mesh is modeled as a solid plate. As we can see, when the DLR wire mesh is modeled as a solid plate, the through-fairing velocity approaches zero. Figures 15–17 suggest that the DLR wire mesh indeed behaves much like a solid plate due to its very fine pores.

V. APPLICATION OF THE DLR WIRE MESH TO THE NOISE REDUCTION OF TANDEM CYLINDERS

The well-known problem of tandem cylinders has been widely studied to explore its noise generation and reduction mechanisms due to its simple geometry but interesting flow and aeroacoustic physics. Meanwhile, it is characterized by typical aerodynamic flow phenomena associated with noise generation of aircraft landing gears. In the tandem cylinder configuration, the pressure fluctuations on the upstream cylinder, caused by vortex shedding, are weaker than those generated on the downstream cylinder by wake-cylinder interaction.[34] Consequently, the downstream cylinder dominates the noise generation and radiation, producing an overall directivity pattern that is similar to that of an isolated cylinder.[34–37] In this section, we study the noise-reduction performances of the DLR wire mesh on tandem cylinders using our model developed in Sec. III C.

During the past two decades, several experiments on the tandem cylinders configuration have been performed by NASA. Experiments by Jenkins *et al.*[38,39] and Neuhart *et al.*[40] have been performed in the Basic Aerodynamic Research Tunnel (BART) at NASA Langley Research Center, providing cylinder surface pressure, hot-wire measurements in the wake, etc. The diameter of the cylinders used in the experiments was $D = 0.057\,15$ m. The cylinders had the same span as the BART wind tunnel, i.e., $L_z/D = 12.4$. The separation distance between the two cylinders' axes was $L_c/D = 3.7$. The freestream velocity was set to 44 m/s to achieve a Reynolds number of 1.66×10^5 based on the cylinder diameter. To ensure a fully turbulent vortex shedding, the boundary layers on the upstream cylinder were tripped between azimuthal positions of 50° and 60° from the leading stagnation point using a transition strip. Experimental data are available for cases with only the upstream cylinder tripped and with both cylinders tripped, the latter being denoted as C2 Trip in this paper.

The above-mentioned tandem cylinder arrangement tested in the BART was also investigated in NASA LaRC's anechoic wind tunnel, the quiet flow facility (QFF). Cylinder surface pressure, velocity in the wake, and noise spectra in the far field were measured in the QFF. The cylinders spanned the 0.914 m section, yielding an aspect ratio of $L_z/D = 16$. In the QFF measurements, the tripping of boundary layers on cylinder surfaces was duplicate. These experimental data, achieved in both the BART and QFF, were presented at the benchmark problems for air frame noise computations (BANC) workshop (see Lockard[41] for a review). The experimental data on the cylinder surface pressure, velocity in the wake, and far-field noise spectra will be used to validate the present simulation of tandem cylinders.

Recently, some other experiments on the tandem cylinder configuration, in the framework of the EU H2020 IMAGE project, were

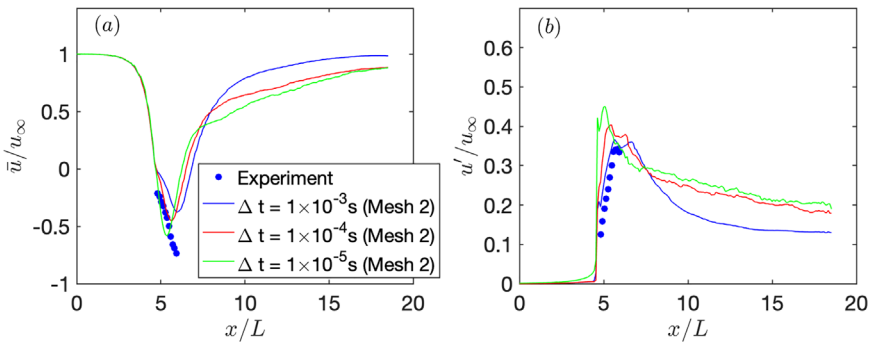

FIG. 11. Flow statistics along the line at the intersection of planes $y/H = 0.356$ and $z/H = 0.5$: (a) mean streamwise velocity and (b) turbulent intensity. In the simulations, the proposed model in Eqs. (24) and (26) is applied and three different time steps are used.

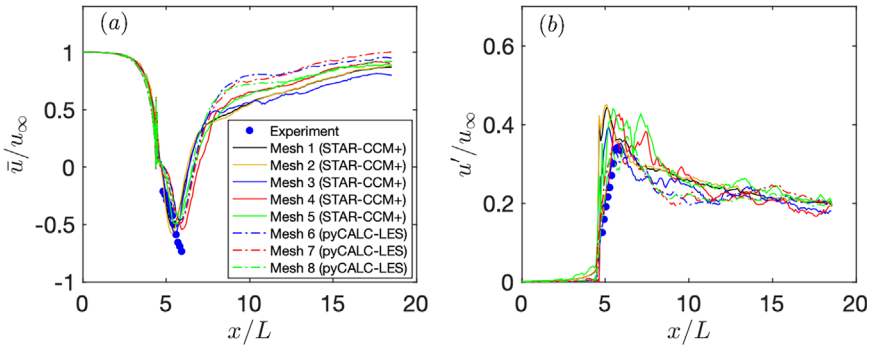

FIG. 13. Flow statistics along the line at the intersection of planes $y/H = 0.356$ and $z/H = 0.5$: (a) mean streamwise velocity and (b) turbulent intensity. In the simulations, the proposed model in Eqs. (24) and (26) is applied and different solvers and meshes are used.

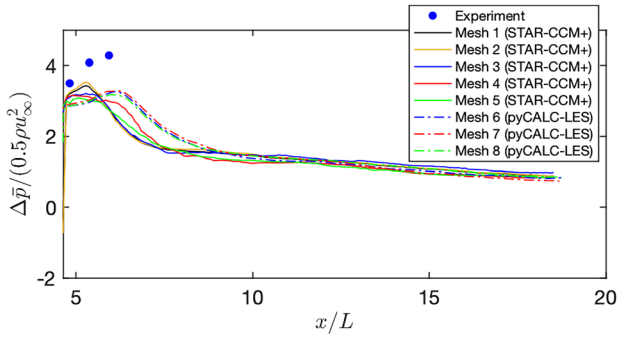

FIG. 14. Pressure drop along the line at the intersection of planes $y/H = 0.356$ and $z/H = 0.5$. In the simulations, the proposed model in Eqs. (24) and (26) is applied and different solvers and meshes are used.

conducted.[14,15,18] Due to technical constraints of the wind tunnel (blockage effect), the diameter of the cylinders was reduced to $D = 0.04$ m. The aspect ratio of tandem cylinders in the wind tunnel reported in the IMAGE project was $L_z/D = 10$. As a consequence, the freestream velocity was increased to $U_0 = 63$ m/s in order to have the same Reynolds number as in the BART and QFF experiments. The separation distance between the two cylinders' axes in the experiments reported in the IMAGE project remained the same as the BART and QFF experiments, i.e., $L_c/D = 3.7$. The directivity of the overall sound pressure level (OASPL) achieved in the IMAGE project will be used to validate the present numerical prediction.

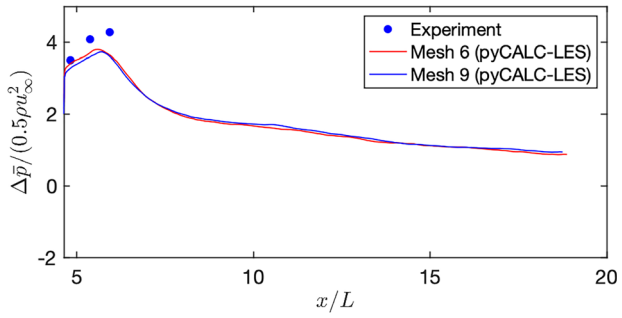

FIG. 16. Pressure drop along the line at the intersection of planes $y/H = 0.356$ and $z/H = 0.5$. In the simulations, the DLR wire mesh is modeled as a solid plate.

In the present numerical simulations, we adopt the flow conditions in the IMAGE project with a span of $L_z/D = 3$. The computational domain is a cylindrical domain with a diameter of $42D$ and a spanwise length of $L_z = 3D$. The boundary condition in the spanwise direction is periodic. The origin (0, 0) of the coordinate system is located at the center of the upstream cylinder [see Fig. 18(a)]. The computational mesh is a trimmed mesh, together with prism layers near the cylinder surfaces. The trimmed cell size of the mesh varies within the computational domain, from 1 mm in the cylinder near wake to 80 mm in the farthest field. As a result, in the cylinder near wake region, there are 120 grid points in the spanwise direction. This mesh has also been successfully used to simulate turbulent flows past tandem cylinders in the IMAGE project.[42] Figure 18 shows a sketch of the computational domain and

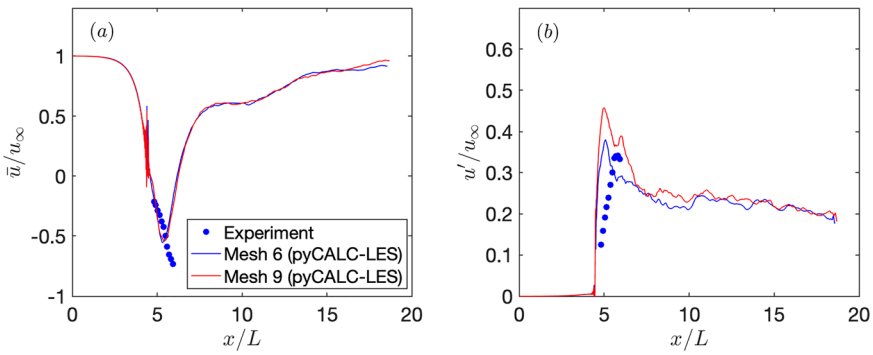

FIG. 15. Flow statistics along the line at the intersection of planes $y/H = 0.356$ and $z/H = 0.5$: (a) mean streamwise velocity and (b) turbulent intensity. In the simulations, the DLR wire mesh is modeled as a solid plate.

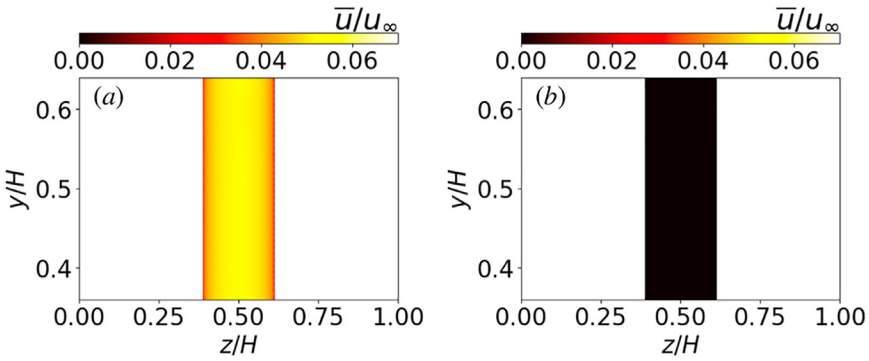

FIG. 17. Streamwise velocity on the cross section at $x = x_{fairing}$: (a) the proposed model in Eqs. (24) and (26) and (b) the model when the DLR wire mesh is treated as a solid plate. Both simulations are performed on mesh 6 by pyCALC-LES.

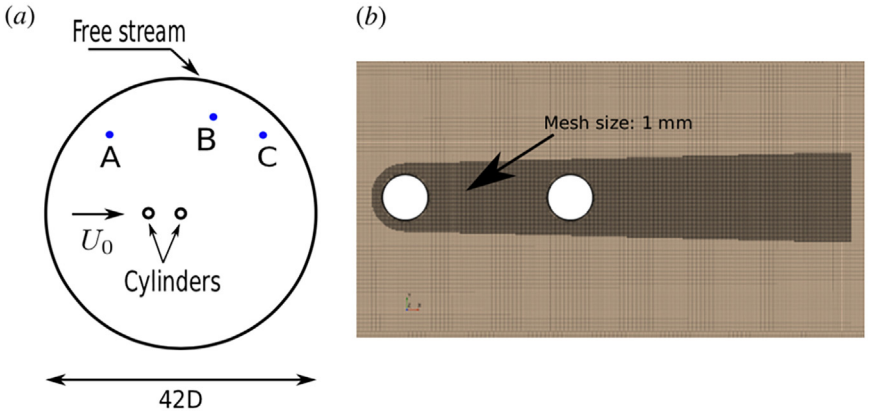

FIG. 18. The baseline configuration for tandem cylinders: (a) sketch of computational domain with three probes A $(-8.33D, 27.82D)$, B $(9.11D, 32.49D)$, and C $(26.55D, 27.82D)$ and (b) computational mesh near the cylinders. The boundary condition in the spanwise direction is periodic. The origin of the coordinate system is located at the center of the upstream cylinder.

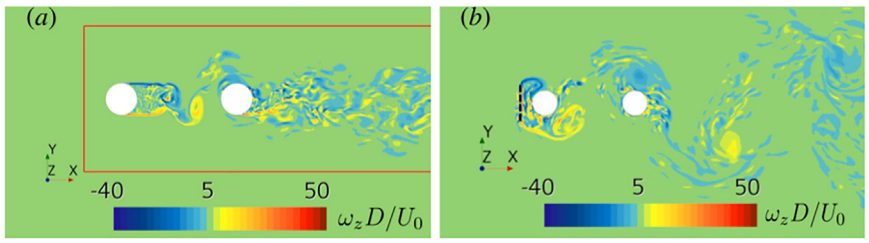

FIG. 19. Instantaneous vorticity: (a) baseline configuration with the FW-H integral surface and (b) Conf. 1 with the DLR wire mesh highlighted at $x/D = -1$.

a close-up view of the computational mesh near the cylinders. The flow solver, including the computational aero-acoustics (CAA) part, is the commercial Siemens STAR-CCM+. The compressible Navier–Stokes equations are solved in a coupled manner. The far-field noise is then computed by integrating the noise sources on a permeable integral surface according to the Ffowcs Williams–Hawkings (FW-H) analogy. A second-order bounded central-difference (BCD) scheme for the convective flux is adopted and an implicit time marching method with a time step of $\Delta t = 5 \times 10^{-5}$ s is used to advance the physical time. Time-averaged quantities (e.g., velocity in the wake, cylinder surface pressure) as well as instantaneous quantity (e.g., noise in the far field) are collected to validate against the experimental data. Figure 19 shows snapshots of the instantaneous vorticity for the baseline case and Conf. 1 (see Table II) using the DLR wire-mesh model in Eqs. (24) and (26). The wire mesh is located at $1D$ upstream the center of the upstream cylinder, as shown in Fig. 19(b).

TABLE II. Wire mesh (WM) dimensions and grid size.

Case	WM width	WM span	# M. cells
Baseline	/	/	29
Configuration 1	$1.5D$	$3D$	46
Configuration 2	$1.5D$	$1.5D$	31
Configuration 3	$5D$	$0.9D$	39

Table II shows parameters for the baseline tandem cylinders and three cases using the DLR wire-mesh model. The number of cells in these computational meshes ranges from 29×10^6 to 46×10^6. The

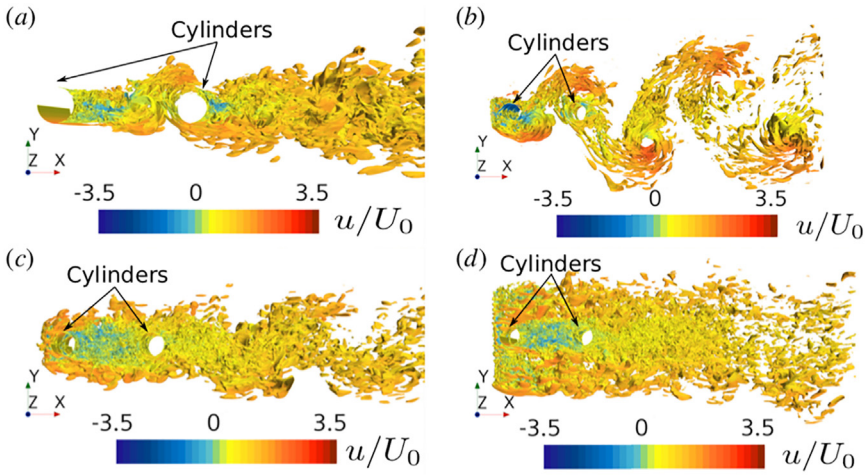

FIG. 20. Instantaneous streamwise velocity on isosurface of $\omega_z D/U_0 = 1.25$: (a) baseline case, (b) Conf. 1, (c) Conf. 2, and (d) Conf. 3.

wake downstream of the cylinders is much broader in Conf. 1. Therefore, the mesh is refined to a further distance in the cross-stream direction from the wake centerline, resulting in a bigger mesh. In Conf. 1, the DLR wire mesh has the same span as the tandem cylinders with a width of 1.5D. Conf. 2 has the same width as Conf. 1 but with a shorter span of 1.5D. Conf. 3 has a larger width of 5D with a smaller span of 0.9D, leading to the same total area as Conf. 1. For Conf. 2 and 3, the screen spanwise length is 50% and 30% of the spanwise length of the cylinders, respectively.

Figure 20 shows the instantaneous streamwise velocity on the isosurface of $\omega_z D/U_0 = 1.25$. In the baseline configuration shown in Fig. 20(a), large-scale roll-up of the shear layers emanating from the upstream cylinder is observed, similar to the shear-layer growth of an isolated circular cylinder.[37] The vortex shedding from the upstream cylinder then interacts with the downstream cylinder, producing a significant amount of noise which is the dominant noise source in this configuration.[34] In Conf. 1 shown in Fig. 20(b), the vortex street generated by the DLR wire mesh is scattered by the upstream cylinder to form a broader vortex street, which later interacts with the downstream cylinder, resulting in an even broader vortex street and more small-scale vortices. It is clear that the unsteady turbulent wake oscillates more strongly in this configuration. As a result, as will be seen in Figs. 24 and 25, noise is increased rather than reduced in this configuration. In Conf. 2 and 3 shown in Figs. 20(c) and 20(d), as the DLR wire mesh does not span the full spanwise length $L_z = 3D$ of the computational domain, a portion of fluid passes beside the DLR wire mesh in the spanwise direction. Thus, the flow does not strongly accelerate above and below (in the vertical direction) the DLR wire mesh, leading to less oscillating turbulent wakes.

Figure 21 shows the time-averaged streamwise velocity along the centerline, $y = 0$, in the wakes of both cylinders. In the gap region between the upstream and downstream cylinders, the predicted velocity agrees reasonably well with the BART particle image velocimetry (PIV) measurement with a large field of view (LFOV), except that the velocity is slightly over-predicted at $x/D < 1.25$ and $x/D > 2$. In the wake region downstream of the downstream cylinder, experimental data are available with both the LFOV and a smaller field of view with better resolution. It is observed that the predicted velocity deviates from the BART LFOV measurement but agrees well with the BART measurement (with the smaller field of view) in which the downstream cylinder is tripped.

Figure 22 shows the pressure coefficient (C_p) on both cylinders. On the upstream cylinder surface, the predicted pressure coefficient distribution is in good agreement with the experimental data. At the

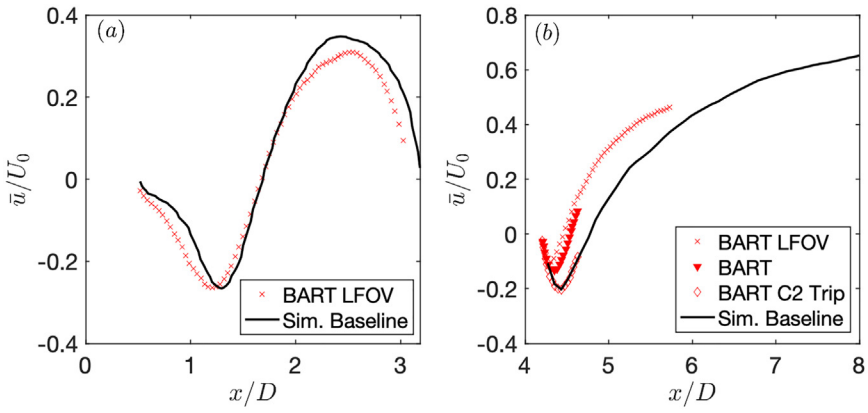

FIG. 21. Time-averaged streamwise velocity along the centerline in the wakes of both cylinders: (a) upstream cylinder and (b) downstream cylinder.

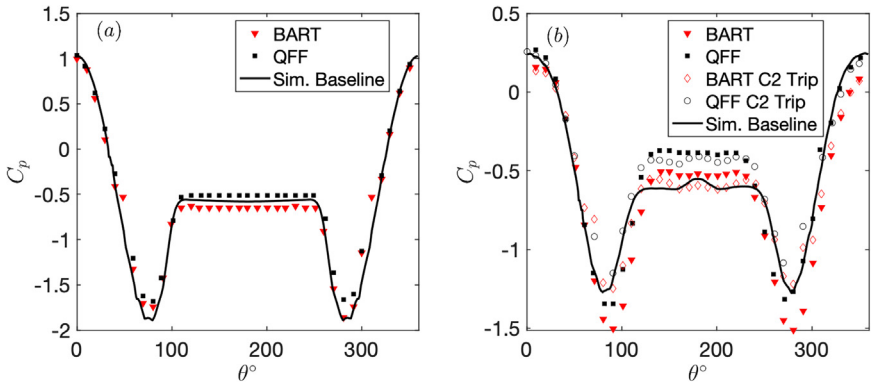

FIG. 22. Time-averaged pressure coefficient (C_p) on both cylinders: (a) upstream cylinder and (b) downstream cylinder.

suction peaks, the prediction agrees better with the QFF experiment. On the downstream cylinder surface, there are two sets of experimental data for each tunnel based on whether or not the downstream cylinder was tripped. Compared to the experimental data with the downstream cylinder not tripped, the present simulation underpredicts the pressure suction peaks. However, despite the wake impingement on the downstream cylinder, tripping still plays an important role in the distribution of pressure coefficient. The experimental data with the downstream cylinder tripped have less negative C_p values at the suction peaks, in better agreement with the present simulation.

In order to confirm that the adopted temporal resolution is sufficient for the study of noise reduction performances of the DLR wire mesh, an additional simulation on the baseline configuration is performed at a much smaller time step $\Delta t = 5 \times 10^{-6} s$. Figure 23 shows the spectra of sound pressure level (SPL) of the far-field noise at three probes A $(-8.33D, 27.82D)$, B $(9.11D, 32.49D)$, and C $(26.55D, 27.82D)$ for baseline simulations using two different time steps, $\Delta t = 5 \times 10^{-5}$ and $\Delta t = 5 \times 10^{-6}$s. It should be noted that the SPLs for all tandem cylinder simulations (including those with a DLR wire mesh) have been corrected, according to the method of Kato *et al.*[43] with an equivalent coherent length of $5.8D$,[15] owing to the fact that the span of tandem cylinders (i.e., $L_z = 3D$) used in the present simulations is different from NASA's experimental one (i.e., $L_z = 16D$). Additionally, due to the Mach-number difference between the present simulations and the NASA measurement, the power spectral density (PSD) used to compute the SPL has also been corrected according to a M^6 scaling for all simulation cases. Overall, the simulation using the smaller time step $\Delta t = 5 \times 10^{-6} s$ accurately predicts the sound spectra in the whole frequency range at all probe locations. For the larger time step $\Delta t = 5 \times 10^{-5} s$, the present numerical simulation agrees very well with the experiment over a large span of frequencies, particularly at lower frequencies including the dominant tone at $St = 0.22$. However, it is also observed that there is an underprediction between the present simulated baseline simulation and the NASA's experiment at high frequencies ($St > 2$). The reason is related to an increasing numerical dissipation at (very) high frequencies, upon the time step adopted, as seen in other similar simulations. Nevertheless, since the dominant tone in the tandem cylinder configuration is at $St = 0.22$ and noise at high frequencies beyond $St > 2$ is much quieter (about 60 dB lower) than the dominant tone, the spatial and temporal resolution adopted in the present simulations is sufficient for the study of noise reduction performances of the DLR wire mesh. Therefore, to reduce the computational cost, a larger time step $\Delta t = 5 \times 10^{-5} s$ is adopted for the simulations of the three configurations with the DLR wire mesh.

Figure 24 shows the spectra of SPL of the far-field noise at three probes A, B, and C for all configurations, obtained using the porous FW-H approach. In terms of the configurations with the DLR wire mesh applied, Conf. 1 increases noise at both lower and higher frequencies. A louder tone at a lower frequency ($St = 0.09$) is observed.

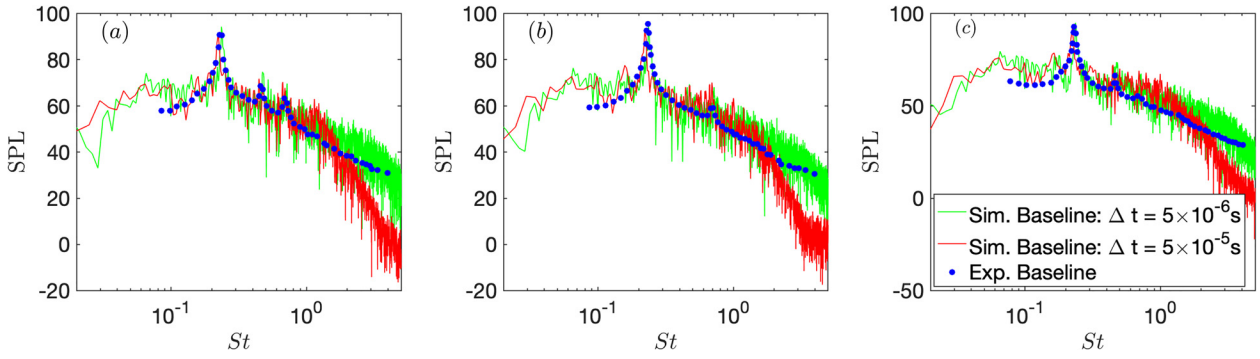

FIG. 23. Comparison of spectra of sound pressure level of far-field noise at three probes in simulations using two different time steps: (a) probe A, (b) probe B, and (c) probe C. The experimental data for the baseline configuration, taken from Terracol and Manoha,[18] was measured in the QFF wind tunnel by NASA.

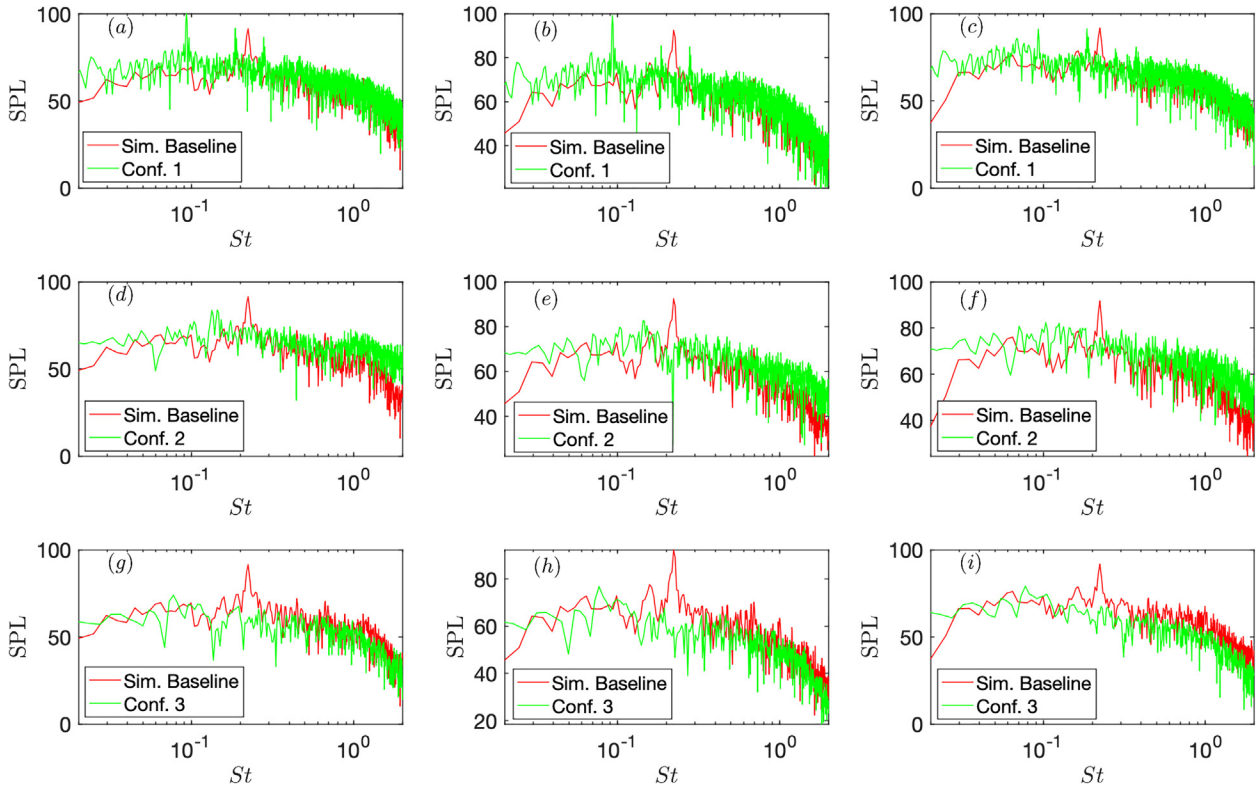

FIG. 24. Spectra of sound pressure level of far-field noise at three probes A (left column), B (middle column), and C (right column).

This low-frequency tone is generated by the strong vortex shedding from the DLR wire mesh itself. Conf. 2 slightly increases noise at lower frequencies as well as higher frequencies in comparison with the baseline configuration. However, the original dominant tone of tandem cylinders at $St = 0.22$ is significantly reduced. In addition, the highest peak at $St = 0.09$ disappears when compared to Conf. 1. Conf. 3 significantly reduces the original tone of tandem cylinders at $St = 0.22$. Moreover, the noise is reduced at frequencies higher than the dominant frequency. This is more obvious at the downstream probe C. Meanwhile, at low frequencies, the noise level remains almost the same as that of the baseline tandem cylinders.

Figure 25 shows the far-field sound radiation directivity of overall sound pressure level (OASPL) for all configurations. The OASPL is defined as

$$\mathrm{OASPL} = 20\log_{10}\left(\frac{p'_{rms}}{p_{ref}}\right), \tag{27}$$

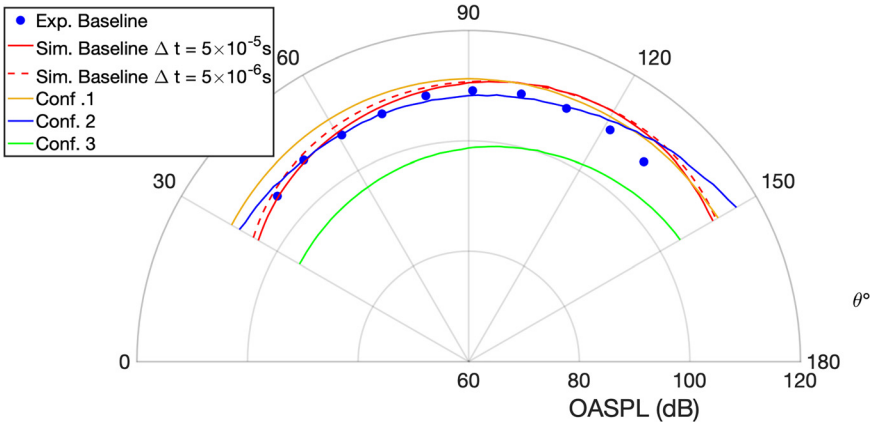

FIG. 25. Comparison of far-field noise directivity between the baseline configuration and configurations 1–3. The sampling probes are on a circular arc centered at the upstream cylinder axis with a diameter of 37.5*D*. The experimental data for the baseline configuration, taken from Terracol and Manoha,[18] were measured in the IMAGE project.

where p'_{rms} is the root mean square sound pressure fluctuation and $p_{ref} = 2 \times 10^{-5}$ Pa is the reference pressure. Similar to the SPLs in Fig. 24, the OASPLs for all simulation cases have also been corrected, according to the method of Kato *et al.*[43] with an equivalent coherent length of 5.8D (Zhu *et al.*[15]), owing to the fact that the present simulated span of tandem cylinders (i.e., $L_z = 3D$) is different from the experiment conducted in the IMAGE project (i.e., $L_z = 10D$). Regarding the baseline tandem cylinders, the agreement between the present simulation and the experimental data achieved in the IMAGE project is satisfactory, with better agreement at upstream observer angles. Regarding the configurations with the DLR wire mesh applied, Conf. 1 slightly reduces the OASPL between observer angles $\theta = 100°$ and 140°. However, noise level is increased at upstream observer positions. Conf. 2 slightly reduces the OASPL between $\theta = 54°$ and 130° but also slightly increases noise at observer angles outside this range. Compared to the baseline configuration, Conf. 3 significantly reduces the OASPL at all observed angles, with a reduction of 7–8 dB at upstream and downstream observer positions and up to 12 dB in the middle observer positions.

Although Conf. 1 and Conf. 2 do not show a significant noise reduction and the most efficient noise reduction compared to the baseline configuration is observed for Conf. 3, it is interesting to note that, in our recent numerical study on noise reduction of aircraft landing gears using the above DLR wire mesh model (results not shown here), noise is significantly reduced using a narrow but long-span DLR wire mesh similar to Conf. 1, consistent with the microphone measurements conducted at A-Tunnel of Delft University of Technology in the Netherlands, within the framework of the European Union's INVENTOR project. The reason is that the DLR wire mesh itself in Conf. 1 is almost as noisy as the tandem cylinders but is quieter than an aircraft landing gear. Therefore, applying a DLR wire mesh similar to Conf. 1 is able to reduce the noise generated by a landing gear. Figure 26 shows the DLR wire mesh (in Conf. 1 situation) self-noise (i.e., without the presence of the tandem cylinders) in comparison with the noise generated by the baseline tandem cylinders. As can be seen, at low frequencies, the wire mesh itself is much louder than the tandem cylinders, particularly at the downstream probe C, where the level of the low-frequency wire mesh self-noise is almost as high as the dominant tone of the tandem cylinders.

VI. CONCLUDING REMARKS

In this paper, we model a novel wire mesh consisting of very fine wires and pores. This wire mesh has recently been tested to be very efficient in reducing LG noise, according to a set of microphone measurements recently conducted at A-Tunnel of Delft University of Technology in the Netherlands, within the framework of the European Union's on-going INVENTOR project.

Due to the large difference in dimension between the LG and the wire-mesh pores, detailed meshing of the geometry and the wire mesh is not practical since it will result in a large amount of computational cells. A numerical model for the wire mesh is, thus, imminently needed. To develop a numerical model for this wire mesh, a set of experimental flow-field data have been deployed for the model validation. The experimental data were measured in the WAABLIEF wind tunnel with only 22% of the wind-tunnel cross section covered by the wire mesh, taking into account the vortex shedding from both sides of the wire-mesh fairing. Although a source term for the momentum equations, proportional to the square of flow velocity, has been proposed and successfully applied to model wire meshes with relatively large wires (e.g., 1 mm) and lattices (e.g., 4 mm) in the IMAGE project,[14,15] it is found that these existing models do not reproduce the aforementioned experiments well when applied to the novel DLR wire mesh. To overcome this limitation, we additionally introduce a linear term proportional to the flow velocity to account for the permeability of the wire mesh, based on another set of experiments with the wind-tunnel cross section fully covered by the wire mesh. This yields a better prediction of the mean flow, turbulence and pressure drop in comparison with the experimental data measured in the WAABLIEF wind tunnel. Since a significant portion of the air passes over the wire-mesh fairing from the side edges of the fairing instead of passing through the wire-mesh pores, the permeability of the wire-mesh fairing is important and, thus, should be characterized by the additionally introduced linear term.

The DLR wire mesh is modeled with different number of cells in the flow-through direction to represent the wire mesh. It is found that with four or more cells used, very similar results are achieved. It is also found that the results obtained using 10 and 14 cells overlap, suggesting the convergence of the modeling results. In addition, the DLR wire mesh is represented with both the physical and nonphysical thicknesses. Results show that both forms of thicknesses impose

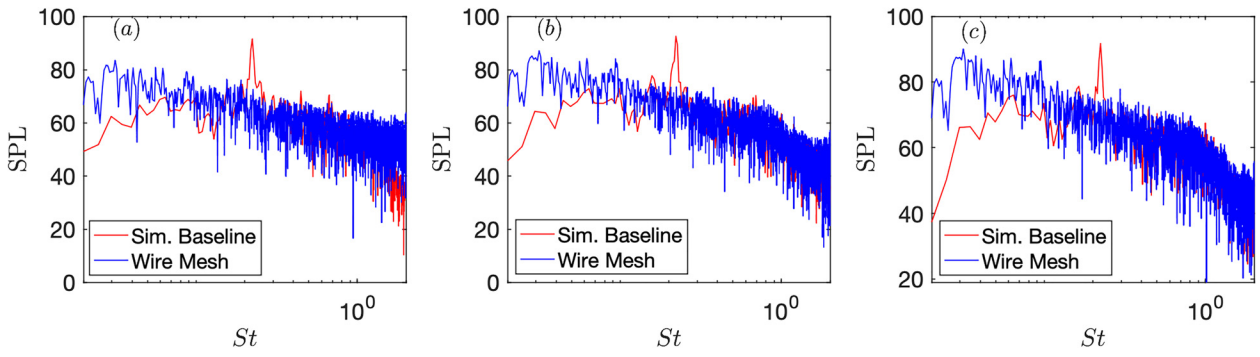

FIG. 26. Comparison between the far-field noise of the baseline tandem cylinders and the DLR wire mesh (in Conf. 1 situation) self-noise at three probes: (a) probe A, (b) probe B, and (c) probe C.

insignificant influences. Simulation results using different computational meshes show that the proposed model for the DLR wire mesh neither requires grid refinement at the fairing nor depends on the mesh type as long as the same total force term is added. Two different solvers, the commercial STAR-CCM+ and the in-house code pyCALC-LES, produce essentially similar results, although pyCALC-LES gives a somewhat delayed peak of pressure drop. Finally, the DLR wire mesh is modeled as a solid plate, showing that unlike the ONERA wire mesh,[17,18] the DLR wire mesh performs much like a solid fairing.

Of the three configurations with the DLR wire mesh model deployed for the tandem cylinders, the most efficient noise reduction with respect to the baseline configuration is observed for Conf. 3 in which a wide but short-span DLR wire mesh is deployed. Conf. 3 is able to eliminate the original dominant tone at $St = 0.22$. Moreover, the SPL is reduced at higher frequencies, but not beyond $St = 2$. As a result, the OASPL is reduced by 7–8 dB at upstream and downstream observer angles and up to 12 dB in the middle observer angles. With Conf. 1, which implements a narrow but long-span DLR wire mesh, a tone is triggered at a lower frequency and the SPL is overall increased, due to the fact that the strong vortex shedding generated by the DLR wire mesh itself interacts with the downstream cylinder which induces additional noise generation. With Conf. 2, which implements a narrow but short-span DLR wire meshes, the SPL is slightly increased at lower frequencies as well as at higher frequencies. However, the original dominant tone of tandem cylinders at $St = 0.22$ is significantly reduced. Overall, noise is not reduced, although there are slight noise reductions at some observer angles.

In summary, a numerical model is proposed for a novel wire mesh consisting of very fine wires and pores. In future work, this wire-mesh model will be applied to complex landing gears including brakes and a torque link, to study the reduction of LG noise. Since the proposed model is limited to wire meshes at zero angle of incidence, it should be generalized to enable the modeling of wire meshes at any arbitrary angles of incidence in the future. In addition, characterizing the permeability of the DLR wire mesh through a set of experiments may also be conducted in the future.

ACKNOWLEDGMENTS

This work was supported by the project Innovative Design of Installed Airframe Components for Aircraft Noise Reduction ("INVENTOR," European Union's Horizon 2020 Research and Innovation Programme, under Grant Agreement No. 8605383). The computations were enabled by resources provided by the Swedish National Infrastructure for Computing (SNIC) partially funded by the Swedish Research Council through Grant Agreement No. 2018-05973. Our INVENTOR partners, Dr. Riccardo Zamponi at the von Karman Institute for Fluid Dynamics and Dr. Fabien Méry at the Office National d'Etudes et de Recherches Aérospatiales, are gratefully acknowledged for providing their experimental data used in this paper. Dr. S. Wasala at Trinity College Dublin is gratefully acknowledged for sharing his simulation file on the baseline tandem cylinders conducted in the previous IMAGE project.

AUTHOR DECLARATIONS

Conflict of Interest

The authors have no conflicts to disclose.

Author Contributions

Shuai Li: Conceptualization (equal); Formal analysis (equal); Investigation (equal); Methodology (equal); Software (equal); Validation (equal); Visualization (equal); Writing – original draft (equal); Writing – review & editing (equal). **Lars Davidson:** Conceptualization (equal); Formal analysis (equal); Funding acquisition (equal); Investigation (equal); Methodology (equal); Software (equal); Supervision (equal); Validation (equal); Visualization (equal); Writing – review & editing (equal). **Shia-Hui Peng:** Conceptualization (equal); Funding acquisition (equal); Supervision (equal); Writing – review & editing (equal).

DATA AVAILABILITY

The data supporting the findings in this study are available from the corresponding author upon reasonable request.

REFERENCES

[1]W. Dobrzynski, "Almost 40 years of airframe noise research: What did we achieve?" J. Aircraft **47**, 353–367 (2010).
[2]J.-F. Piet, R. Davy, G. Elias, H. Siller, L. Chow, C. Seror, and F. Laporte, "Flight test investigation of add-on treatments to reduce aircraft airframe noise," AIAA Paper No. 2005-3007, 2005.
[3]K. Boorsma, X. Zhang, and N. Molin, "Perforated fairings for bluff body noise control," AIAA Paper No. 2007-3462, 2007.
[4]K. Boorsma, X. Zhang, and N. Molin, "Landing gear noise control using perforated fairings," Acta Mech. Sin. **26**, 159–174 (2010).
[5]G. J. Bennett, J. Lai, G. O'Brien, D. Ragni, F. Avallone, and M. Pott-Pollenske, "Flow control and passive low noise technologies for landing gear noise reduction," AIAA Paper No. 2022-2848, 2022.
[6]K. Zhao, P. Okolo, E. Neri, P. Chen, J. Kennedy, and G. J. Bennett, "Noise reduction technologies for aircraft landing gear—A bibliographic review," Prog. Aerosp. Sci. **112**, 100589 (2020).
[7]Y. Xu, Z.-Y. Li, J.-J. Wang, and L.-J. Yang, "On the interaction between turbulent vortex rings of a synthetic jet and porous walls," Phys. Fluids **31**, 105112 (2019).
[8]S. Oerlemans, C. Sandu, N. Molin, and J.-F. Piet, "Reduction of landing gear noise using meshes," AIAA Paper No. 2010-3972, 2010.
[9]M. Smith, L. Chow, and N. Molin, "Control of landing gear noise using meshes," AIAA Paper No. 2010-3974, 2010.
[10]C. Chen and X. Li, "Microscopic fluid dynamics of a wire screen bound to a slit resonator excited by acoustic waves," Phys. Fluids **32**, 116107 (2020).
[11]P. N. Okolo, K. Zhao, J. Kennedy, and G. J. Bennett, "Numerical assessment of flow control capabilities of three dimensional woven wire mesh screens," Eur. J. Mech.-B **76**, 259–271 (2019).
[12]P. N. Okolo, K. Zhao, J. Kennedy, C. Mgbemena, M. Eke, and G. J. Bennett, "Two-dimensional simplification of complex three-dimensional wire mesh screens," J. Aerosp. Eng. **34**, 04021098 (2021).
[13]P. N. Okolo, K. Zhao, J. Kennedy, and G. J. Bennett, "Mesh screen application for noise reduction of landing gear strut," AIAA Paper No. 2016-2845, 2016.
[14]W. Zhu, Z. Xiao, and S. Fu, "Simulations of turbulence screens for flow and noise control in tandem cylinders," Red **105**, 1 (2019), https://www.eucass.eu/9-news/79-eucass-2019-dois-of-full-papers-2.
[15]W. Zhu, Z. Xiao, and S. Fu, "Numerical modeling screen for flow and noise control around tandem cylinders," AIAA J. **58**, 2504–2516 (2020).
[16]P. N. Okolo, K. Zhao, J. Kennedy, and G. J. Bennett, "Numerical modeling of wire screens for flow and noise control," AIAA Paper No. 2017-3700, 2017.
[17]M. Terracol and E. Manoha, "Development of a wire mesh screen model for unsteady simulation of noise reduction devices, with application to the tandem cylinder configuration," AIAA Paper No. 2018-3473, 2018.
[18]M. Terracol and E. Manoha, "Numerical wire mesh model for the simulation of noise-reduction devices," AIAA J. **59**, 987–1007 (2021).

[19]P. Roach, "The generation of nearly isotropic turbulence by means of grids," Int. J. Heat Fluid Flow **8**, 82–92 (1987).
[20]T. Kurian and J. H. Fransson, "Grid-generated turbulence revisited," Fluid Dyn. Res. **41**, 021403 (2009).
[21]E. Rice, "A model for the acoustic impedance of linear suppressor materials bonded on perforated plate," in *7th Aeroacoustics Conference* (AIAA, Palo Alto, 1981), p. 1999.
[22]N. Van de Wyer, A. Zapata, D. Nogueira, and C. F. Schram, "Development of a test rig for the measurement of turbulent boundary layer wall pressure statistics," AIAA Paper No. 2018-3122, 2018.
[23]R. Zamponi, E. Gallo, A. Zarri, J. de Decker, Y. C. Küçükosman, and C. Schram, "Characterization of the flow through innovative permeable fairings at the VKI WAABLIEF facility," Zenodo, 2022.
[24]A. Minotti, F. Simon, and F. Gantié, "Characterization of an acoustic liner by means of laser Doppler Velocimetry in a subsonic flow," Aerosp. Sci. Technol. **12**, 398–407 (2008).
[25]M. Fabien and S. Delphine, "Aerodynamic characterisation of porous fairings: Pressure drop and laser Doppler Velocimetry measurements," Zenodo, 2022.
[26]Siemens Digital Industries Software, *Simcenter STAR-CCM+, Version 2021.1* (Siemens, 2021).
[27]L. Davidson, "pyCALC-LES: A python code for DNS, LES and hybrid LES-RANS" (Chalmers University of Technology, Gothenburg, 2021).
[28]Siemens Digital Industries Software, *Simcenter STAR-CCM+ User Guide v. 2021.1* (Siemens, 2021).
[29]S. B. Pope and S. B. Pope, *Turbulent Flows* (Cambridge University Press, 2000).
[30]R. Zamponi, S. Satcunanathan, S. Moreau, D. Ragni, M. Meinke, W. Schröder, and C. Schram, "On the role of turbulence distortion on leading-edge noise reduction by means of porosity," J. Sound Vib. **485**, 115561 (2020).
[31]C. Teruna, F. Manegar, F. Avallone, D. Ragni, D. Casalino, and T. Carolus, "Noise reduction mechanisms of an open-cell metal-foam trailing edge," J. Fluid Mech. **898**, A18 (2020).
[32]C. Teruna, L. Rego, F. Avallone, D. Ragni, and D. Casalino, "Applications of the multilayer porous medium modeling approach for noise mitigation," J. Aerosp. Eng. **34**, 04021074 (2021).
[33]N. Nishiyama and T. Yokoyama, "Permeability of porous media: Role of the critical pore size," J. Geophys. Res.: Solid Earth **122**, 6955–6971, https://doi.org/10.1002/2016JB013793 (2017).
[34]D. Lockard, M. Khorrami, M. Choudhari, F. Hutcheson, T. Brooks, and D. Stead, "Tandem cylinder noise predictions," AIAA Paper No. 2007-3450, 2007.
[35]G. A. Brès, D. Freed, M. Wessels, S. Noelting, and F. Pérot, "Flow and noise predictions for the tandem cylinder aeroacoustic benchmark," Phys. Fluids **24**, 036101 (2012).
[36]O. Inoue and N. Hatakeyama, "Sound generation by a two-dimensional circular cylinder in a uniform flow," J. Fluid Mech. **471**, 285–314 (2002).
[37]S. Li, D. E. Rival, and X. Wu, "Sound source and pseudo-sound in the near field of a circular cylinder in subsonic conditions," J. Fluid Mech. **919**, A43 (2021).
[38]L. Jenkins, M. Khorrami, M. Choudhari, and C. McGinley, "Characterization of unsteady flow structures around tandem cylinders for component interaction studies in airframe noise," AIAA Paper No. 2005-2812, 2005.
[39]L. Jenkins, D. Neuhart, C. McGinley, M. Khorrami, and M. Choudhari, "Measurements of unsteady wake interference between tandem cylinders," AIAA Paper No. 2006-3202, 2006.
[40]D. Neuhart, L. Jenkins, M. Choudhari, and M. Khorrami, "Measurements of the flowfield interaction between tandem cylinders," AIAA Paper No. 2009-3275, 2009.
[41]D. Lockard, "Summary of the tandem cylinder solutions from the benchmark problems for airframe noise computations-I workshop," AIAA Paper No. 2011-353, 2011.
[42]S. Wasala, S.-H. Peng, L. Davidson, L. González-Gutiérrez, and A. Morán-Guerrero, "Modelling of DBD plasma actuator for controlling noise from a tandem cylinders configuration," in *INTER-NOISE and NOISE-CON Congress and Conference Proceedings* (Institute of Noise Control Engineering, 2019), Vol. 259, pp. 876–888.
[43]C. Kato, A. Iida, Y. Takano, H. Fujita, and M. Ikegawa, "Numerical prediction of aerodynamic noise radiated from low Mach number turbulent wake," AIAA Paper No. 93-0145, 1993.